A TWO-PHASE DEBRIS-FLOW MODEL THAT INCLUDES COUPLED EVOLUTION OF VOLUME FRACTIONS, GRANULAR DILATANCY, AND PORE-FLUID PRESSURE

DAVID L. GEORGE[(*)] & RICHARD M. IVERSON[(*)]

[(*)] U.S. Geological Survey, 1300 SE Cardinal Ct., Vancouver - WA 98683 USA
Email: dgeorge@usgs.gov - riverson@usgs.gov

ABSTRACT

Pore-fluid pressure plays a crucial role in debris flows because it counteracts normal stresses at grain contacts and thereby reduces intergranular friction. Pore-pressure feedback accompanying debris deformation is particularly important during the onset of debris-flow motion, when it can dramatically influence the balance of forces governing downslope acceleration. We consider further effects of this feedback by formulating a new, depth-averaged mathematical model that simulates coupled evolution of granular dilatancy, solid and fluid volume fractions, pore-fluid pressure, and flow depth and velocity during all stages of debris-flow motion. To illustrate implications of the model, we use a finite-volume method to compute one-dimensional motion of a debris flow descending a rigid, uniformly inclined slope, and we compare model predictions with data obtained in large-scale experiments at the USGS debris-flow flume. Predictions for the first 1 s of motion show that increasing pore pressures (due to debris contraction) cause liquefaction that enhances flow acceleration. As acceleration continues, however, debris dilation causes dissipation of pore pressures, and this dissipation helps stabilize debris-flow motion. Our numerical predictions of this process match experimental data reasonably well, but predictions might be improved by accounting for the effects of grain-size segregation.

KEY WORDS: *debris flow, dilatancy, pore pressure*

INTRODUCTION

One of the greatest challenges in debris-flow modeling involves seamlessly simulating behavior during initiation and subsequent rapid flow. Most numerical simulations of debris-flow motion avoid this challenge by specifying finite force imbalances in static debris poised on slopes. In this way, modelers artificially impose a static state before computations begin. By contrast, initiation of natural debris flows occurs when balanced forces are infinitesimally perturbed -- that is, when the factor of safety in static debris becomes infinitesimally smaller than 1. As motion of the debris begins, however, the force imbalance may significantly change because dilatancy and pore-pressure feedback modify frictional resistance. This feedback commonly determines whether motion evolves to produce a rapid debris flow or a different phenomenon, such as a landslide that creeps imperceptibly downslope (IVERSON *et alii,* 2000; WANG & SASSA, 2003; IVERSON, 2005). Similar feedback is also important during later stages of debris-flow motion, because it can cause frictional resistance to evolve in response to changing stresses and deformation rates.

Here we summarize a new, depth-averaged computational model that simulates debris-flow motion from initiation to post-depositional consolidation by including the effects of coupled evolution of dilatancy, solid and fluid volume fractions, and pore-fluid pressure. This formulation results in a hyperbolic system of four simultaneous partial differential

415

equations we solve numerically by using a finite-volume wave-propagation method similar to that used in CLAWPACK and GEOCLAW (LeVeque, 2002; Berger *et alii*, in press?). We implement the computations in a new FORTRAN code we call DIGCLAW, and we compare solutions generated by DIGCLAW with aggregated data obtained in large-scale experiments at the USGS debris-flow flume.

MODEL FORMULATION

To emphasize physical concepts and minimize mathematical complexity, we focus on one-dimensional motion of a two-dimensional debris flow descending a rigid, impermeable plane uniformly inclined at the angle θ (Figure 1). The flow moves downslope as an evolving surge that has a characteristic length, L, characteristic thickness, H, and characteristic grain diameter, δ, such that $L \gg H \gg \delta$. The disparity of these length scales justifies our use of a depth-averaged continuum model.

Our model treats debris as a mixture of incompressible solid grains of mass density ρ_s occupying the volume fraction m and incompressible fluid of mass density ρ_f occupying the volume fraction 1-m, such that the mixture bulk density is

$$\rho = \rho_s m + \rho_f (1\text{-}m) \qquad (1)$$

In DIGCLAW the depth-averaged solid volume fraction $\overline{m}$ is a dependent variable that evolves as a function of the downslope coordinate, x, and time, t, implying that the depth-averaged bulk density, $\overline{\rho}$, also evolves. The other dependent variables are the depth-averaged downslope flow velocity, $\overline{v}(x,t)$, the flow thickness, $h(x,t)$, and the basal pore-fluid pressure, $p_{bed}(x,t)$ (Figure 1).

Our model emphasizes motion of the granular solid phase, and treats fluid flow in a frame of reference that moves with the solids. This approach utilizes an apparent fluid velocity $\vec{q}$ (*i.e.*, fluid volume flux per unit area) relative to the solids, defined as

$$\vec{q} = (\vec{v}_f - \vec{v}_s)(1 - m) \qquad (2)$$

where $\vec{v}_f$ and $\vec{v}_s$ are the velocities of the fluid and solids, respectively, in a fixed frame of reference (Bear, 1972). Formally, the model assumes that the magnitude of $\vec{q}$ is sufficiently small that $||\vec{q}|| \ll ||\vec{v}_s||(1\text{-}m)$, although violation of this assumption (*e.g.*, when $\vec{v}_s = 0$) poses no significant problem, provided that variation of $\vec{q}$ has negligible effect on the mass-weighted mixture velocity, defined as

$$\vec{v} = [\vec{v}_s \rho_s m + \vec{v}_f \rho_f (1 - m)] / \rho \qquad (3)$$
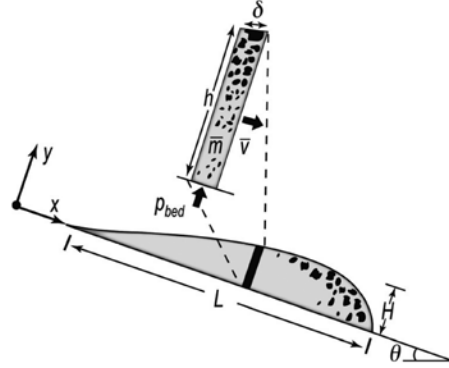
Fig. 1 - Schematic illustrating a debris flow of characteristic length L, characteristic thickness H, and characteristic local grain diameter δ descending a uniform slope inclined at the angle θ. Magnified slice illustrates the dependent variables h, $\overline{v}$, $\overline{m}$, and p_{bed} used in DIGCLAW

Relative motion of solid and fluid phases can lead to possible ambiguity in the definition of $h(x,t)$, because in some instances rocks may protrude through a debris flow's free surface, but in other instances all solid grains may be submerged. To avoid this ambiguity we define $h(x,t)$ as the height of a *virtual* free surface, such that the debris-flow mass per unit basal area is $\overline{\rho} h(x,t)$.

EVOLUTION OF MASS DISTRIBUTION

By employing the mixture bulk density defined in (1) and mixture velocity defined in (3), we can utilize a mixture mass-conservation equation in the standard form

$$\partial \rho / \partial t + \nabla^- \rho \vec{v} = 0 \qquad (4)$$

Mass conservation additionally requires that the divergence of $\vec{q}$ must be balanced by a compensating divergence of the grain velocity $\vec{v}_s$ (Iverson, 1997):

$$\nabla^- \vec{q} + \nabla^- \vec{v}_s = 0 \qquad (5)$$

Divergence of $\vec{v}_s$ implies that m evolves, leading to our definition of the depth-averaged granular dilation rate D:

$$D(x,t) = \int_0^h (\nabla^- \vec{v}_s) dy = -\int_0^h \frac{1}{m} \frac{dm}{dt} dy \qquad (6)$$

Here $d / dt = \partial / \partial t + \vec{v}_s \nabla$ denotes a material time derivative that follows motion of the granular phase.

Because we assume that $m = \overline{m}$, we can recast (6) as

$$\frac{d\overline{m}}{dt} = -\frac{D}{h} \overline{m} \qquad (7)$$

where $\overline{d} / \overline{dt} = \partial / \partial t + \overline{v} \nabla$ denotes a depth-averaged material time derivative. Equation (7), which expresses depth-averaged conservation of the granular phase, is the first of the four evolution equations solved by DIGCLAW.

416

We evaluate depth-averaged mass conservation for the two-phase mixture by integrating (4) through the flow depth to find

$$\int_0^h \left(\partial \rho / \partial t + \nabla^- \rho \overline{v} \right) dy$$
$$= \overline{\rho} \left[\frac{\partial h}{\partial t} + \frac{\partial (h\overline{v})}{\partial x} + \frac{h}{\overline{\rho}} \frac{\overline{d}\,\overline{\rho}}{\overline{d}t} \right] = 0 \qquad (8)$$

The term including $d\overline{\rho}/dt$ in (8) accounts for changes in $\overline{\rho}$ due to changes in $\overline{m}$. Use of (1) and (7) in conjunction with the chain rule $\overline{d}\,\overline{\rho}/\overline{d}t = (\overline{d}\,\overline{\rho}/d\overline{m})(\overline{d}\,\overline{m}/\overline{d}t)$ shows that these changes can be expressed by $\overline{d}\,\overline{\rho}/\overline{d}t = -(\rho_s - \rho_f)(D\overline{m})/h$, and substitution of this equation in the second line of (8) leads to

$$\frac{\overline{d}h}{\overline{d}t} = \frac{\overline{\rho} - \rho_f}{\overline{\rho}} D - h \frac{\partial \overline{v}}{\partial x} \qquad (9)$$

This depth-averaged mass-conservation equation for the mixture is the second evolution equation solved by DIGCLAW. If $D = 0$, then (9) reduces to the standard depth-averaged mass conservation equation for incompressible materials, and (7) reduces to the trivial relation $\overline{d}\,\overline{m} / \overline{d}t = 0$.

EVOLUTION OF DILATANCY

Although (6), (7), and (9) summarize the kinematic effects of the granular dilation rate, they do not describe the mechanical causes of dilation. For this purpose we use an equation modified slightly from one proposed by IVERSON (2009),

$$\nabla^- \overline{v}_s = \dot{\gamma} \tan \psi - \alpha \frac{d\sigma_e}{dt} \qquad (10)$$

where $\dot{\gamma}$ is the macroscopic shear rate, ψ is the shear-induced dilatancy (a property of granular materials that is commonly expressed as an angle, $-\pi/2 \leq \psi \leq \pi/2$), α is the mixture compressibility (a property that commonly declines as m increases), and σ_e is the effective normal stress (defined as $\sigma_e = \sigma - p$, where σ is the mean total normal stress and p is the pore-fluid pressure). Positive dilatancy indicates that densely packed grains move apart as they shear past one another, whereas negative dilatancy implies that grains converge during shearing, provided that σ_e is constant.

If no macroscopic shearing occurs (i.e., $\dot{\gamma} = 0$), then (10) reduces to a standard equation used in quasi-static soil consolidation theories; but if shearing occurs in a closed container that enforces $\Delta \overline{v}_s = 0$, then (10) reduces to $d\sigma_e/dt = \dot{\gamma} \tan \psi/\alpha$. This equation erroneously predicts that σ_e increases with time if $\psi > 0$ and shearing proceeds at a constant rate $\dot{\gamma}$, thereby demonstrating that

ψ cannot be a material constant. Rather, ψ must evolve and ultimately become zero during steady shearing. In classical soil mechanics, where $\dot{\gamma} < 0.01$ s^{-1} is typical, such steady states are called critical states (SCHOFIELD & WROTH, 1968). In DIGCLAW quasi-steady states with $\psi = 0$ can develop even if $\dot{\gamma} >> 0.01$ s^{-1} .

To calculate evolution of ψ we adopt a rationale similar to that of PAILHA & POULIQUEN (2009), who combined the principles of critical-state soil mechanics with those of dense grain-flow mechanics (FORTERRE & POULIQUEN, 2008) to postulate that the value of $\tan \psi$ depends linearly on $m - m_{eq}$, where m_{eq} is a value of m equilibrated with the ambient state of stress and shear rate. To gauge the effects of the stress state and shear rate on m_{eq}, they used a dimensionless parameter N that can be interpreted as a timescale ratio in which the numerator is the characteristic time for local grain rearrangement (mediated by pore-fluid viscosity, μ), and the denominator is the characteristic time for bulk shear deformation, $1/\dot{\gamma}$ (cf. COURRECH DU PONT et alii, 2003; CASSAR et alii, 2005). Here we identify the grain-rearrangement timescale as $\mu / (\overline{\rho} - \rho_f)gh \cos \theta$, where $(\overline{\rho} - \rho_f) gh \cos \theta$ is the characteristic effective normal stress, and we combine this timescale with the depth-averaged bulk shearing timescale $1/\dot{\gamma} = h/\overline{v}$ to express N as

$$N = \frac{\mu \overline{v}}{(\overline{\rho} - \rho_f)gh^2 \cos \theta} \qquad (11)$$

This relationship shows that N is essentially the reciprocal of the friction number introduced previously to describe the stress state in debris flows (IVERSON & LAHUSEN , 1993; IVERSON, 1997).

Next we define ψ by using the linear PAILHA-POULIQUEN (2009) formula

$$\tan \psi = C_1 \left[\overline{m} - \overline{m}_{eq} \right] \qquad (12)$$

but we include nonlinear dependence of on N:

$$\overline{m}_{eq} = \overline{m}_{crit} (1 - C_2 \tanh N) \qquad (13)$$

Here C_1 and C_2 are positive coefficients that require calibration (cf. PAILHA & POULIQUEN, 2009), and $\overline{m}_{crit}$ is the static, critical-state value of $\overline{m}_{eq}$ that applies when the stress is lithostatic, the pore pressure is hydrostatic, and $N = 0$. As N increases from 0 to ∞, tanh N increases almost linearly from 0 until it smoothly asymptotes to 1, implying that the equilibrium volume fraction $\overline{m}_{eq}$ decreases monotonically but not indefinitely in response to decreasing normal stresses and increasing shear rates. Through its dependence on $\overline{m}_{eq}$ and N, ψ evolves in response to evolution of all of the dependent variables in DIGCLAW: $\overline{m}$, $\overline{v}$, h, and p_{bed}.

417

EVOLUTION OF PORE-FLUID PRESSURE

Development of a depth-averaged evolution equation for p_{bed} involves several steps. The first entails use of a linear, Darcian drag formula to relate $\vec{q}$ to the gradient of excess pore-fluid pressure, p_e:

$$\vec{q} = -(k/\mu)\nabla p_e \tag{14}$$

Here $p_e = p - \rho_f g(h-y)\cos\theta$, where p is the total fluid pressure, and k is the intrinsic hydraulic permeability of the granular debris (BEAR, 1972). A linear drag formula such as (14) may oversimplify the effects of complex phase-interaction forces in debris flows, but detailed investigations of similar mixtures indicate that it probably provides a suitable first approximation (e.g., JOHNSON *et alii*, 1990; SHAMY & ZEGHAL, 2005).

Substitution of (14) into (5) yields a fundamental equation that shows how the divergence of $(k/\mu)\nabla p_e$ is related to the granular dilation rate, $\Delta\vec{v}_s$:

$$\nabla\cdot\vec{v}_s = \nabla\cdot\frac{k}{\mu}\nabla p_e \tag{15}$$

Next, $\Delta\vec{v}_s$ can be eliminated from (15) through use of (10). If k/μ is assumed constant (an assumption that is easily relaxed computationally), the resulting equation reduces to

$$\frac{d\sigma_e}{dt} = -\frac{k}{\alpha\mu}\nabla^2 p_e + \frac{\dot{\gamma}\tan\psi}{\alpha} \tag{16}$$

where $k/\alpha\mu$ plays the role of a pore-pressure diffusivity.

From (16) we obtain a forced, advection-diffusion equation governing evolution of p_e by first using the definitions of effective stress and excess pore-fluid pressure to find that $d\sigma_e/dt = d\sigma/dt - dp_e/dt - d[\rho_f g(h-y)\cos\theta]/dt$. Substitution of this equation into (16) yields

$$\frac{dp_e}{dt} - \frac{k}{\alpha\mu}\nabla^2 p_e = \frac{d}{dt}\left[\sigma - \rho_f g(h-y)\cos\theta\right] - \frac{\dot{\gamma}\tan\psi}{\alpha} \tag{17}$$

The forcing terms on the right-hand side of (17) express the evolving effects of the shear-induced dilation rate $\dot{\gamma}\tan\psi$, the mean total stress σ, and the hydrostatic pore-pressure component $\rho_f g(h-y)\cos\theta$. Note that if all of the time derivatives in (17) are zero and $\dot{\gamma}\tan\psi$ is constant, the equation reduces to the steady-state balance $(k/\mu)\nabla^2 p_e = \dot{\gamma}\tan\psi$, which can alternatively be expressed as $-\nabla\cdot\vec{q} = \dot{\gamma}\tan\psi$. This result shows that porosity creation during steady dilation is balanced by a steady influx of fluid that fills the enlarging pores.

The next step in obtaining our pore-pressure evolution equation is depth integration. Preliminary steps involve recasting (17) in terms of the total pore-fluid pressure, $p = p_e + \rho_f g(h-y)\cos\theta$, and invoking shallow-flow scaling that applies if $H/L \ll 1$. This scaling indicates that $\partial^2 p/\partial y^2 \gg \partial^2 p/\partial x^2$ because $\partial^2/\partial y^2$ scales with $1/H^2$, whereas $\partial^2/\partial x^2$ scales with $1/L^2$. Consequent neglect of $\partial^2 p/\partial x^2$ reduces (17) to

$$\frac{dp}{dt} - \frac{k}{\alpha\mu}\frac{\partial^2 p}{\partial y^2} = \frac{d\sigma}{dt} - \frac{\dot{\gamma}\tan\psi}{\alpha} \tag{18}$$

Another step involves use of the approximations $v_y = (y/h)\,dh/dt$ and $v_x = \bar{v}$ to recast the total time derivatives in (18) as $d/dt = \bar{d}/\bar{dt} + (y/h)(\overline{dh}/\overline{dt})\partial/\partial y$ (SAVAGE & IVERSON, 2003). Then (18) can be rewritten as

$$\frac{\bar{d}p}{\bar{dt}} - \frac{k}{\alpha\mu}\frac{\partial^2 p}{\partial y^3} = \frac{\bar{d}\sigma}{\bar{dt}} + \frac{y}{h}\frac{\bar{d}h}{\bar{dt}}\frac{\partial(\sigma-p)}{\partial y} - \frac{\dot{\gamma}\tan\psi}{\alpha} \tag{19}$$

Depth integration of (19) is accomplished term-by-term by using Leibniz' rule and applying the stress-free surface boundary conditions $p(h) = \sigma(h) = 0$, yielding

$$\frac{\bar{d}(\bar{p}h)}{\bar{dt}} - \frac{k}{\alpha\mu}\left[\frac{\partial p}{\partial y}\Big|_{y=h} + \rho_f g\cos\theta\right]$$
$$= \frac{\bar{d}(\bar{\sigma}h)}{\bar{dt}} - (\bar{\sigma} - \bar{p})\frac{\bar{d}h}{\bar{dt}} - \frac{\bar{v}\tan\psi}{\alpha} \tag{20}$$

where $\bar{p}$ denotes the depth average of p, and $\bar{v}/h$ is used to approximate the depth-averaged shear rate. The term $\rho_f g\cos\theta$ arises in (20) from depth integration of the pore-pressure diffusion term in (19) and application of a zero-flux basal boundary condition that requires the pore-pressure gradient at the bed to remain hydrostatic: $[\partial p/\partial y]_{y=0} = -\rho_f g\cos\theta$. The term $-(\bar{\sigma} - \bar{p})\overline{dh}/\overline{dt}$ arises from depth-integrating the term that includes $\partial(\sigma-p)/\partial y$ in (19) by parts. This term cancels some other terms and thereby reduces (20) to

$$\frac{\bar{d}\bar{p}}{\bar{dt}} - \frac{k}{\alpha\mu h}\left[\frac{\partial p}{\partial y}\Big|_{y=h} + \rho_f g\cos\theta\right] = \frac{\bar{d}\bar{\sigma}}{\bar{dt}} - \frac{\bar{v}\tan\psi}{h\alpha} \tag{21}$$

where
$$\bar{\sigma} = \frac{1+\kappa}{4}\bar{\rho}gh\cos\theta + \frac{1-\kappa}{2}\bar{p} \tag{22}$$

is the depth-averaged mean total normal stress, and κ is a longitudinal normal-stress coefficient that equals 1 if the stress state is hydrostatic (IVERSON & DENLINGER, 2001). Equation (21) is a valid, depth-integrated, one-dimensional pore-pressure evolution equation, but it retains two pore-pressure variables, p and $\bar{p}$, rather than the desired variable, p_{bed}.

To express (21) in terms of p_{bed}, approximations of $\bar{p}$ and $[\partial p/\partial y]_{y=h}$ are necessary, and we obtain these approximations by utilizing the assumption that $m = \bar{m}$ at all depths. This assumption implies that $\Lambda\vec{v}_s$ and $\Lambda\vec{q}$ are not functions of y, further implying that $\partial^2 p/\partial y^2$ is not a function of y in (18) and (19). With this stipulation, we solve $\partial^2 p/\partial y^2 = constant$ and employ the hydrostatic basal boundary condition $\partial p/\partial y\,|_{y=0} = -\rho_f g\cos\theta$

and pressure-free surface boundary condition $p(h) = 0$ to find that $p(y)$ satisfies the quadratic equation

$$p = p_{bed}[1 - (y/h)^2] - \rho_f gh\cos\theta[y/h - (y/h)^2] \qquad (23)$$

This equation indicates that temporal evolution of p is represented entirely by the evolving values of the basal pressure $p_{bed}(t)$ and flow thickness $h(t)$. Equation (23) also implies that

$$\overline{p} = \frac{2}{3}p_{bed} - \frac{1}{6}\rho_f gh\cos\theta \qquad \left.\frac{\partial p}{\partial y}\right|_{y=h} = -\frac{2p_{bed}}{h} + \rho_f g\cos\theta \qquad (24)$$

Substitution of (22) and (24) into (21) then yields

$$\frac{dp_{bed}}{dt} = \frac{-6k}{(1+\kappa)\alpha\mu h^2}\left[p_{bed} - \rho_f gh\cos\theta \right]$$
$$+ \frac{3}{2}\left(\frac{1}{2}g\cos\theta\frac{\overline{d}(\overline{\rho}h)}{dt} + \frac{1}{6}\rho_f g\cos\theta\frac{\overline{d}h}{dt} - \frac{2}{1+\kappa}\frac{\overline{v}\tan\psi}{h\alpha} \right) \qquad (25)$$

The derivatives $\overline{d}(\overline{\rho}h)/dt$ and $\overline{d}h/dt$ can be eliminated from the right-hand side of (25) by using the mass-conservation equation (9), yielding the final form of the evolution equation for p_{bed}:

$$\frac{dp_{bed}}{dt} = \frac{-6k}{(1+\kappa)\alpha\mu h^2}\left[p_{bed} - \rho_f gh\cos\theta \right]$$
$$+ \frac{3}{2}\left[\frac{\rho_f}{6\overline{\rho}}(\overline{\rho}-\rho_f)gD\cos\theta - \overline{\rho}gh\cos\theta\left(\frac{\rho_f}{6\overline{\rho}}+\frac{1}{2}\right)\frac{\partial\overline{v}}{\partial x} - \frac{2}{1+\kappa}\frac{\overline{v}\tan\psi}{h\alpha} \right] \qquad (26)$$

The first term on the right-hand side of (26) accounts for pore-pressure relaxation due to the depth-integrated effects of pressure diffusion, and the second term accounts for the forcing effects of the evolving gravitational load and dilation rate.

EVOLUTION OF MOMENTUM DISTRIBUTION

For a debris mixture with $\rho = \overline{\rho}$, depth integration of the left-hand side of the x component of the momentum-conservation equation $(\partial(\rho\overline{v})/\partial t + \nabla \cdot \rho\overline{v}\overline{v})$ yields a result that can be written in several forms, including

$$\int_0^h\left[\frac{\partial(\overline{\rho}v_x)}{\partial t} + \frac{\partial(\overline{\rho}v_x^2)}{\partial x} \right]dy = \frac{\partial(\overline{\rho}h\overline{v})}{\partial t} + \frac{\partial(\overline{\rho}h\overline{v}^2)}{\partial x} + \frac{\partial}{\partial x}\overline{\rho}\int_0^h(v_x-\overline{v})^2dy$$
$$= \overline{\rho}h\frac{\overline{dv}}{dt} + \overline{v}\overline{\rho}\left[\frac{\partial h}{\partial t} + \frac{\partial(h\overline{v})}{\partial x} + \frac{h}{\overline{\rho}}\frac{\overline{d}\overline{\rho}}{dt} \right] \qquad (27)$$
$$= \overline{\rho}\left[\frac{\partial(h\overline{v})}{\partial t} + \frac{\partial(h\overline{v}^2)}{\partial x} \right] - (\overline{\rho}-\rho_f)D\overline{v} \quad .$$

The first line of (27) is exact, but subsequent lines assume that differential advection of x momentum as a function of y is negligible, and therefore omit the integral containing $v_x - \overline{v}$. In the second line of (27), the term in brackets expresses mass conservation and vanishes through application of (8), leaving only the term $\overline{\rho}h(\overline{dv}/dt)$. This term is mathematically correct but physically "non-conservative" because it does not

explicitly represent the effects of evolving $\overline{\rho}h$. The final line of (27), which is used in DIGCLAW, differs from a conventional, conservative shallow-water formulation owing to presence of the term $-(\overline{\rho}-\rho_f)D_v$. This term equals $h\overline{v}(d\overline{\rho}/dt)$ and thereby accounts for the effects of D on evolution of $\overline{\rho}$.

The right-hand side of the depth-averaged momentum-conservation equation expresses the sum of forcing effects due to gravity and resisting effects due to internal and boundary stresses, as derived by IVERSON (1997). Addition of the right-hand side to (27) yields the fourth evolution equation solved by DIGCLAW,

$$\overline{\rho}\left[\frac{\partial(h\overline{v})}{\partial t} + \frac{\partial(h\overline{v}^2)}{\partial x} \right] - (\overline{\rho}-\rho_f)D\overline{v}$$
$$= \overline{\rho}gh\sin\theta - \kappa\overline{\rho}gh\cos\theta\frac{\partial h}{\partial x} - (1-\kappa)h\frac{\partial p_{bed}}{\partial x} - \tau_s - \tau_f \qquad (28)$$

Here τ_s and τ_f are the basal shear tractions exerted by the solid and fluid phases, respectively.

To estimate τ_s we use the Coulomb-Terzaghi equation for granular friction influenced by pore pressure and dilatancy,

$$\tau_s = \sigma_{e\,bed}\tan(\phi_{bed}+\psi) \qquad (29)$$
$$\approx [\overline{\rho}gh\cos\theta - p_{bed}]\tan(\phi_{bed}+\psi)$$

where ϕ_{bed} is the steady-state (zero-dilatancy) friction angle of grains in contact with the bed, $\phi_{bed}+\psi$ is the effective basal friction angle when nonzero dilatancy is present (IVERSON, 2005), and $\overline{\rho}gh\cos\theta - p_{bed}$ is an estimate of the basal effective stress, $\sigma_{e\,bed}$. To estimate τ_f we use

$$\tau_f = (1-\overline{m})\mu\frac{\overline{v}}{h} \qquad (30)$$

where $1-\overline{m}$ is the fluid volume fraction and $\overline{v}/h$ is, again, a depth-averaged approximation of the shear rate $\overline{\dot{\gamma}}$.

MATHEMATICAL CLOSURE

Two additional relationships are needed to evaluate D and κ, and thereby complete the mathematical model. We obtain an equation for D by combining (5), (6) and (15) to find that

$$D = -\int_0^h(\nabla\cdot\frac{k}{\mu}\nabla p_e)dy \qquad (31)$$
$$= -\frac{2k}{\mu h}(p_{bed} - \rho_f gh\cos\theta)$$

The second line of (31) assumes that k/μ is constant and that the pore-pressure distribution obeys the quadratic relationship specified in (23). It also shows that p_{bed} remains equilibrated to the dilation rate D as both quantities evolve. This behavior is a logical consequence of mass conserva-

419

tion in a fully saturated mixture together with our assumptions of Darcian fluid flow and $m = \overline{m}$.

The value of the longitudinal stress coefficient κ generally can vary from about 0.3 to 3, depending on whether flowing debris undergoes longitudinal extension or compression (SAVAGE & HUTTER, 1989; IVERSON, 1997, 2009; IVERSON & DENLINGER, 2001). The effects of such variation are relatively subtle but potentially quite complicated. To avoid such complications while focusing our computations on coevolution of $\overline{m}$, $\overline{v}$, h, and p_{bed}, we have used the traditional shallow-flow assumption, $\kappa = 1$. The most important consequence of this assumption is that the term $(1 - \kappa) h \partial p_{bed}/\partial x$ vanishes from (28), implying that pore-fluid pressure exerts direct effects on flow momentum only through its influence on basal Coulomb friction.

MODEL PREDICTIONS AND TESTS

As a demonstration and test of our model predictions, we have used DIGCLAW to simulate behaviour measured in a series of eight replicate experiments performed in the USGS debris-flow flume. In each experiment 10 m³ of water-saturated sand, gravel and mud ("SGM") discharged abruptly from behind a vertical headgate and travelled more than 70 m down the uniformly sloping (31º), 2-m wide flume before encountering flatter slopes and debouching from the flume mouth. IVERSON *et alii* (2010) presented details of experimental protocols, data acquisition and processing, and debris and flume properties. Because the flume's sidewalls were vertical and much smoother than its bumpy flume bed (1 mm vs. 16 mm characteristic roughness amplitudes), a one-dimensional model was appropriate for simulating flow within the flume. Parameter values used to generate simulation results generally matched values measured in laboratory tests (Tab. 1). A notable exception was the value of k, which we discuss below.

Our DIGCLAW simulations used 1000 fixed, uniformly spaced Eulerian grid cells on a domain ranging from $x = -10.0$ m to $x = 90.0$ m, where $x = 0$ denoted the flume headgate location. The code used explicit computational time steps that were modified adaptively to satisfy a Courant-Friedrichs-Lewy (CFL) condition. At each time step the numerical solution was updated by using a finite-volume wave-propagation method to solve Riemann problems at grid cell interfaces, as detailed elsewhere (*e.g.*, LEVEQUE, 2002;

BERGER *et alii*, in press). The results presented here depict 10 s of debris-flow motion; generation of the results required about 49 s of CPU time on a standard desktop computer with a 2.4 GHz processor.

INITIAL CONDITIONS AND SHORT-TERM BEHAVIOR

We focus first on predicted short-term evolution of the dependent variables h, $\overline{v}$, $\overline{m}$ and p_{bed} in the upper part of the flume, from $x = -5$ m (behind the headgate) to $x = 5$ m, just downslope of the headgate (Figure 2). At $t = 0$, the debris impounded behind the headgate is static and the basal pore-fluid pressure is hydrostatic ($p_{bed} = \rho_f g h \cos \theta$). The solid volume fraction is uniformly $m = 0.61$, matching the mean value measured by IVERSON *et alii* (2010), and implying a loosely packed initial state. The panels of Figure 2 show these initial conditions as well as the evolving longitudinal profiles of all dependent variables at $t = 0.2$, 0.4, 0.6, 0.8 and 1.0 s.

The model predicts that as downslope motion begins, the highest velocities occur near the flow front, resulting in progressive longitudinal extension and decreasing depth of the entire debris mass (Fig. 2 a and b). At the same time, the solid volume fraction increases everywhere except at the leading edge of the advancing flow (Fig. 2c), and this increase causes a commensurately widespread increase in basal pore-fluid pressure, p_{bed} (Figure 2d). At $t = 1$ s, for example, much of the mass has $p_{bed} \sim 10$ kPa and $h \sim 0.5$ m, implying a mostly liquefied state (*i.e.*, $p_{bed} \approx \rho g h \cos \theta$). An exception to this behavior develops in the advancing flow snout, which begins to dilate almost immediately because $h \rightarrow 0$ at the snout tip, and implied shear rates

Parameter (units)	Symbol	Experiment value(s)	Model value
Solid grain density (kg/m³)	ρ_s	2700	2700
Pore-fluid density (kg/m³)	ρ_f	1000-1200	1000
Gravitational acceleration magnitude (m/s²)	g	9.8	9.8
Slope angle (degrees)	θ	31	31
Debris basal friction angle (degrees)	ϕ_{bed}	40	40
Debris hydraulic permeability (m²)	k	4×10^{-12} to 4×10^{-11}	10^{-8}
Pore-fluid viscosity (Pa-s)	μ	0.001 to 0.1	0.05
Debris compressibility(Pa⁻¹)	α	10^{-5}-10^{-3}	10^{-5}
Static critical-state solid volume fraction	m_{crit}	> 0.6	0.62
Dilatancy coefficient 1	C_1	---	0.5
Dilatancy coefficient 2	C_2	---	20

Tab. 1 - Comparison of parameter values used in DIG-CLAW with values measured in "SGM" debris-flow flume experiments of IVERSON et alii (2010)

420
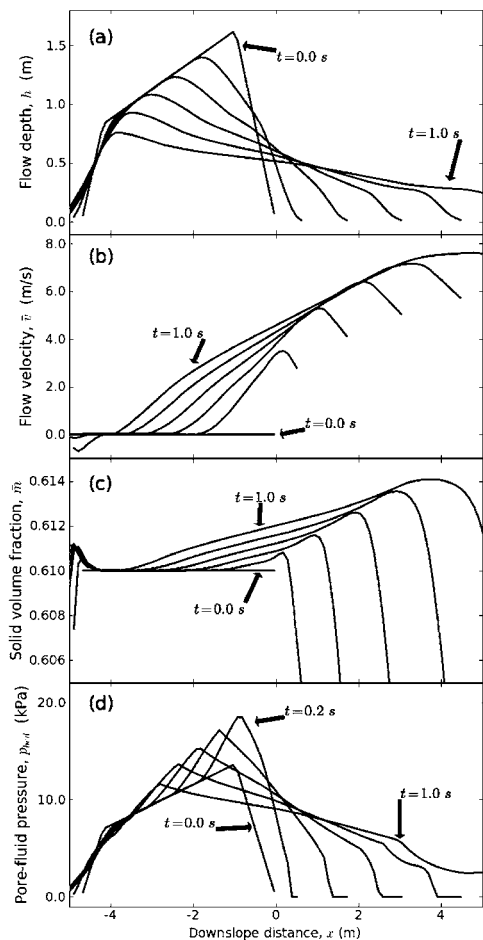
Fig. 2 - Simulated short-term evolution of dependent variables over the interval from x = −5 m to 5 m. Longitudinal profiles of variables are shown for the initial condition (t =0) and for t= 0.2, 0.4, 0.6, 0.8, and 1.0 s

Fig. 3 - Simulated long-term evolution of dependent variables over the interval from x = -10 m to 75 m. Longitudinal profiles are shown for the initial condition (t =0) and for t= 2, 4, 6, 8, and 10 s

are accordingly high. As the solid volume fraction in the snout declines in response to high shear rates, pore pressures there also decline. Flow resistance therefore begins to grow in the snout while most of the trailing debris maintains a liquefied state that allows it to push the snout from behind. As a consequence, the snout initially moves downslope faster than an ideal frictionless body, despite its relatively high flow resistance.

DOWNSLOPE BEHAVIOR

Behavior computed as the simulated flow moves further downslope differs qualitatively from short-term behavior because flow velocities become high enough that the dominant debris response becomes dilative (Figure 3). In conjunction with dilation, ba-

sal pore pressures gradually relax from their elevated values, and effective basal friction increases. Meanwhile, the flow elongates greatly while maintaining a steep leading edge, or snout, as observed in experiments (IVERSON *et alii*, 2010). The peak flow depth occurs just behind the snout and gradually declines until it stabilizes at about $h = 0.1$ m (Figure 3a), while the snout speed stabilizes at between 8 and 10 m/s (Figure 3b), similar to behavior observed in the experiments (IVERSON *et alii*, 2010). The high speed of the snout leads to commensurately large shear rates, dilation rates, and rates pore-pressure depletion, thereby reinforcing the frictional resistance of the snout. As a consequence, classic head-and-tail debris-flow architecture develops and persists.

421

COMPARISON OF COMPUTED AND MEASU-RED TIME SERIES

Next we compare model predictions with values of flow depth, $h(t)$, basal pore-fluid pressure, $p_{bed}(t)$, and total basal normal stress, $\sigma_{bed}(t)$ measured in the eight replicate SGM experiments described by Iverson *et alii* (2010). Aggregated data from replicate experiments provide a better basis for model tests than do data from individual experiments or field observations, because data aggregation minimizes the effects of idiosyncrasies and reveals the effects of inherent variability. Therefore, Figure 4 superposes model predictions (black lines) on gray shaded envelopes that depict mean values ±1 standard deviation measured in eight experiments.

Figure 4 compares model predictions with time series measured at two instrumented cross sections: one 32 m downslope from the flume headgate and one 66 m downslope from the headgate. All panels of the figure show that model predictions of flow-front arrival times differ from measured arrival times by

< 1 s. Viewed in more detail, the evolving values of predicted flow depth $h(t)$ and basal total normal stress $\sigma_{bed}(t)$ at $x = 32$ m match those of data relatively well (Figure 4 a and b), but the predicted basal pore-fluid pressure $p_{bed}(t)$ is somewhat lower than measured values (Figure 4c). At $x = 66$ m, the predictions of flow depth and basal normal stress remain relatively good, but the predicted pore-fluid pressure is considerably smaller than that observed in experiments. The next section discusses some shortcomings of the model that might account for these discrepancies.

DISCUSSION

In our simulations of debris-flow flume experiments, values of some parameters were not precisely constrained by independent measurements. When we adjusted the values of these parameters within the range of physically plausible values, it affected our predictions, but we did not make such adjustments blindly.
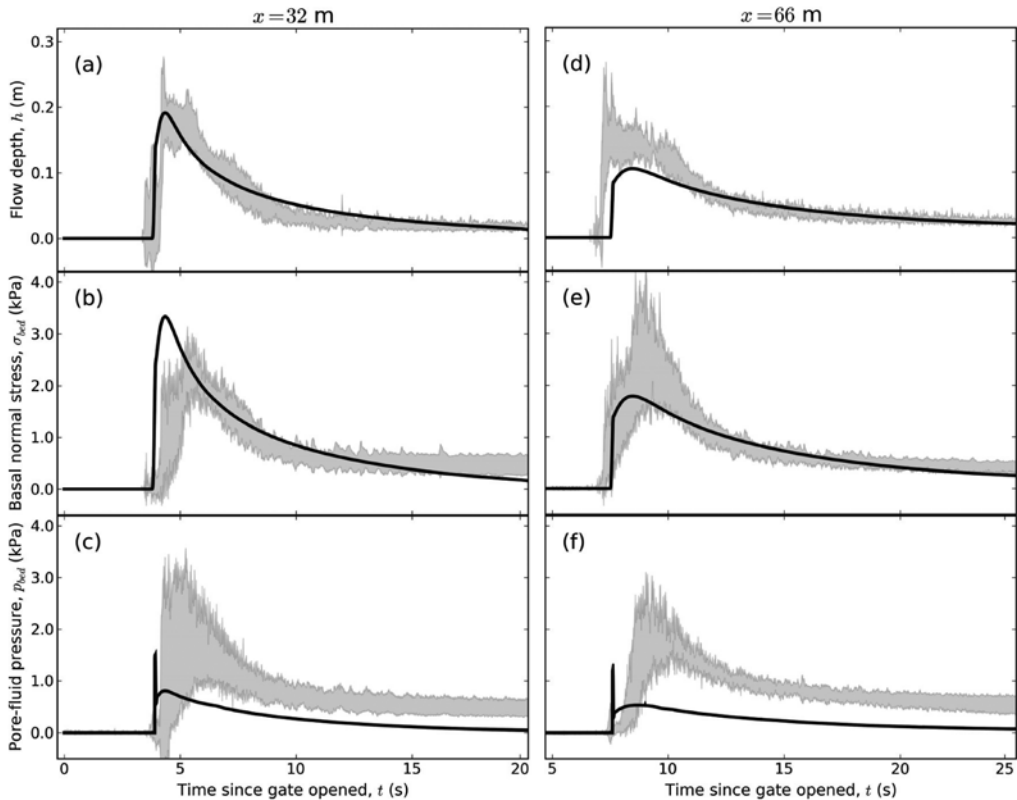
Fig. 4 - Comparison of model predictions (black lines) and aggregated time series data (gray shaded areas) measured at two instrumented cross sections in the SGM debris-flow flume experiments of IVERSON et alii (2010). The shaded areas depict the mean values +/- one standard deviation of measurements made in eight replicate experiments

422

5th International Conference on Debris-Flow Hazards Mitigation: Mechanics, Prediction and Assessment   Padua, Italy - 14-17 June 2011

Initially, when we began simulating the flume experiments, we found that the model predicted flow velocities almost twice as large as those observed at $x = 66$ m. The high velocities were due to widespread persistence of very high pore-fluid pressures, such that friction remained close to zero. By increasing the ratio k / μ to values about five times larger than those measured in quasistatic permeameter tests with water-saturated SGM, we caused pore pressures to relax more rapidly toward hydrostatic levels. This adjustment increased basal friction enough to produce reasonably accurate predictions of flow speeds. We believe the adjustment is defensible from a physical perspective, because rapidly shearing, dilated debris is likely to be more permeable than debris at rest in a permeameter.

Additionally, we followed the precedent established by Pailha & Pouliquen (2009) and selected values of the dilatancy coefficients C_1 and C_2 to optimize model fits to the data. Interestingly, however, despite the fact that many aspects of our model differ from those of the Pailha-Pouliquen (2009) model, our values $C_1 = 0.5$ and $C_2 = 20$ are comparable to the values $C_1 = 4.09$ and $C_2 = 25$ used by Pailha & Pouliquen to optimize their fits to data from small-scale, underwater granular avalanches. (Note that in the Pailha-Pouliquen formulation, K_3 is analogous to our C_1, and K_2 is analogous to our C_2.) This consistency lends some credibility to the formulae that employ C_1 and C_2 for calculating the dilatancy angle ψ (i.e., equations (12) and (13).

The most significant discrepancy between our model predictions and measured flow behavior involves relaxation of basal pore-fluid pressure. In our predictions the pressure relaxes more rapidly than the measured pressure, but as noted above, this rapid relaxation is necessary to obtain realistic flow speeds. We believe the lack of grain-size segregation in our model is responsible for this problem. In experimental debris flows, and in most natural debris flows, large grains rapidly concentrate at flow fronts, focussing more flow resistance there while leaving finer-grained tails that remain largely liquefied (Iverson, 2003). Thus, as segregation occurs, the permeability k can increase significantly in coarse-grained flow fronts, leading to a zone of almost completely depleted basal pore-fluid pressure. This heterogeneous architecture develops to some degree in our computations, but we believe that size segregation would enhance this development and lead to attendant regulation of flow speeds. Recent work on grain-size segregation in dry granular avalanches (e.g., Gray & Ancey, 2009) may point the way toward including segregation effects in our debris-flow model.

CONCLUSION

Our model differs from previous models of debris-flow dynamics by describing coupled evolution of dilatancy, solid and fluid volume fractions, pore-fluid pressure, and flow depth and velocity. This formulation enables use of realistic initial conditions with infinitesimal force imbalances, and it therefore permits seamless simulation of debris-flow initiation and subsequent flow. A key feature of our model is non-monotonic evolution of computed pore pressures during initiation (when pressures tend to increase and promote liquefaction) and subsequent flow (when pressures tend to relax diffusively). This non-monotonic evolution results from evolution of the dilatancy angle and volume fractions in response to changes in the debris' stress state and shear rate.

By computing simultaneous evolution of several variables, our model provides more detailed predictions than most alternative models, and it therefore facilitates more stringent testing. Our model predictions of evolving flow depths and velocities match experimental data quite well, but to attain these matches, our computations require use of a relatively high debris permeability that leads to overprediction of pore-pressure relaxation. This shortcoming might be remedied by including grain-size segregation effects that lead to evolving permeability distributions and sharper differences in debris-flow head and tail friction. At present, however, we are encouraged that our model predictions match many aspects of debris-flow behavior measured in large-scale experiments.

REFERENCES

BEAR J. (1972) - *Dynamics of fluids in porous media*. Dover, New York.

BERGER M.J., GEORGE D.L., LEVEQUE R.J. & MANDLI K.T. (in press) - *The GEOCLAW software for depth-averaged flows with adaptive refinement, Adv*. Water Resources.

CASSAR C., NICOLAS M. & POULIQUEN O. (2005) - *Submarine granular flows down inclined planes*. Physics of Fluids, **17**: 103301.

COURRECH DU PONT S., GONDRET P., PERRIN B. & RABAUD M. (2003) - *Granular avalanches in fluids*. Physical Rev. Let., **90**: 044301.

FORTERRE Y. & POULIQUEN O. (2008) - *Flows of dense granular media*. Annual Rev. Fluid Mech., **40**: 1-24.

GRAY J.M.N.T & ANCEY C. (2009) - *Segregation, recirculation and deposition of coarse particles near two-dimensional avalanche fronts*. J. Fluid Mech., **629**: 387-423 doi:10.1017/S0022112009006466.

IVERSON R.M. (1997) - *The physics of debris flows*. Reviews of Geophysics, **35**: 245-296.

IVERSON R.M. (2003) - *The debris-flow rheology myth*. In RICKENMANN D. & CHEN C.-L., EDS., *Debris-flow Hazards Mitigation: Mechanics, Prediction, and Assessment,* v. **1**:303-314, Millpress, Rotterdam,.

IVERSON R.M. (2005) - *Regulation of landslide motion by dilatancy and pore-pressure feedback*. J. Geophys. Res., **110**: F02015 doi: 10.1029/2004JF000268.

IVERSON R.M. (2009) - *Elements of an improved model of debris-flow motion*. Powders and Grains 2009 (Proc. Sixth Intl. Conf. Micromech. Granular Media), M. Nakagawa and S. Luding, eds., Amer. Inst. Physics, Melville, New York, 9-16.

IVERSON R.M. & DENLINGER R.P. (2001) - *Flow of variably fluidized granular masses across three-dimensional terrain: 1. Coulomb mixture theory*. J. Geophys. Res., **106**: 537-552.

IVERSON R.M. & LAHUSEN R.G. (1993) - *Friction in debris flows: inferences from large-scale flume experiments*. Hydraulic Engineering `93 (Proc. 1993 Conf. Hydr. Div. Amer. Soc. Civil Engineers) v. **2**: 1604-1609.

IVERSON R.M., LOGAN M., LAHUSEN R.G. & BERTI M. (2010) - *The perfect debris flow? aggregated results from 28 large-scale experiments*. J. Geophys. Res., **115**: F03005 doi:10.1029/2009JF001514.

IVERSON R.M., REID M.E., IVERSON N.R., LAHUSEN R.G., LOGAN M., MANN J.E., & BRIEN D.L. (2000) - *Acute sensitivity of landslide rates to initial soil porosity.* Science, **290**: 513-516.

JOHNSON G., MASSOUDI M. & RAJAGOPAL K.R. (1990) - *A review of interaction mechanisms in fluid-solid flow*s, Tech. Rep. DOE/PETC/TR-90/9, U.S. Dep. of Energy, Pittsburgh Energy Tech. Ctr., Pittsburgh, USA, 54 pp.

LEVEQUE R.J. (2002) - *Finite volume methods for hyperbolic problems*. Cambridge Univ. Press, Cambridge, U.K.

PAILHA M. & POULIQUEN O. (2009) - *A two-phase flow description of the initiation of underwater granular avalanches*. J. Fluid Mech., **633**: 115-135 doi:10.1017/S0022112009007460.

SAVAGE S.B. & HUTTER K. (1989) - *The motion of a finite mass of granular material down a rough incline*. J. Fluid Mech., **199**: 177-215.

SAVAGE S.B. & IVERSON R.M. (2003) - *Surge dynamics coupled to pore-pressure evolution in debris flows*. In: RICKENMANN D. & CHEN C.-L., EDS. *Debris-flow Hazards Mitigation: Mechanics, Prediction, and Assessment*. vol. **1**: 503-514, Millpress, Rotterdam,

SCHOFIELD A.N. & WROTH C.P. (1968) - *Critical State Soil Mechanics*. London, McGraw-Hill.

SHAMY U.E. & ZEGHAL M. (2005) - *Coupled continuum-discrete model for saturated granular materials*. J. Engrg. Mech., **131**: 413-426.

WANG G. & SASSA K. (2003) - *Pore-pressure generation and movement of rainfall-induced landslides: effects of grain size and fine-particle content*. Eng. Geology, **69**: 109-125.

424

5th International Conference on Debris-Flow Hazards Mitigation: Mechanics, Prediction and Assessment   Padua, Italy - 14-17 June 2011